



# Structural and compositional data for childrenite from the Homolka granite, Czech Republic

Jonas Toupal<sup>1</sup>, Daniela Mauro<sup>2,3</sup>, Cristian Biagioni<sup>2,4</sup>, Federica Zaccarini<sup>5</sup>, and Reto Gieré<sup>1,6</sup>

<sup>1</sup>Department of Earth and Environmental Science, University of Pennsylvania,  
Philadelphia, PA 19104-6316, USA

<sup>2</sup>Dipartimento di Scienze della Terra, Università di Pisa, Via S. Maria 53, 56126 Pisa, Italy

<sup>3</sup>Museo di Storia Naturale, Università di Pisa, Via Roma 79, 56011 Calci (PI), Italy

<sup>4</sup>Centro per l'Integrazione della Strumentazione scientifica dell'Università di Pisa, Pisa, Italy

<sup>5</sup>Geosciences Programme, Faculty of Science, University Brunei Darussalam, Jalan Tungku Link,  
Gadong, Bandar Seri Begawan BE1410, Brunei

<sup>6</sup>Center of Excellence in Environmental Toxicology, University of Pennsylvania,  
Philadelphia, PA 19104-6316, USA

**Correspondence:** Jonas Toupal (toupal@sas.upenn.edu)

Received: 26 September 2023 – Revised: 6 November 2023 – Accepted: 15 November 2023 – Published: 4 January 2024

**Abstract.** Members of the childrenite–eosphorite series, ideally  $(\text{Fe}_{1-x}\text{Mn}_x)\text{AlPO}_4(\text{OH})_2 \cdot \text{H}_2\text{O}$ , from the highly evolved Homolka granite, in the southern Czech Republic, were characterized using a multi-analytical approach. They occur as anhedral grains, up to  $\sim 0.2$  mm in size, associated with quartz, muscovite, albite, and K-feldspar. Tiny inclusions of probable uraninite have been observed. Backscattered electron images reveal a patchy zoning of these members of the childrenite–eosphorite series, related to an uneven distribution of Fe and Mn. On the basis of electron microprobe analysis, the average composition of the studied material is  $(\text{Fe}_{0.68}\text{Mn}_{0.28}\text{Ca}_{0.03})_{\Sigma 0.99}\text{Al}_{0.96}(\text{P}_{1.04}\text{Si}_{0.01})_{\Sigma 1.05}\text{O}_{4.00}(\text{OH})_{2.09} \cdot 0.91\text{H}_2\text{O}$ , thus corresponding to childrenite. Unit-cell parameters of this species are  $a = 6.9226(9)$ ,  $b = 10.4081(13)$ ,  $c = 13.3957(17)$  Å. Its crystal structure was refined in the space group *Cmca* down to  $R_1 = 0.0295$  on the basis of 602 unique reflections with  $F_o > 4\sigma(F_o)$  and 66 refined parameters. The crystal structure analysis agrees with the results of electron microprobe analysis and suggests that, in the studied material, Fe occurs in the divalent oxidation state only. Crystal structure data are also consistent with the Raman spectrum collected on the same grain that was structurally characterized, confirming the occurrence of  $\text{PO}_4$  groups only in childrenite.

## 1 Introduction

The minerals childrenite, discovered in 1823 (Brooke, 1823), and eosphorite, first described in 1878 (Bush and Dana, 1878), form a solid-solution series (e.g., da Costa et al., 2005; Hurlbut Jr., 1950; Fransolet, 1980). Members of the childrenite–eosphorite series have been reported to occur in hydrothermally altered pegmatites with an LCT (Li–Cs–Ta) geochemical signature as well as in altered, highly evolved granites from several places, including Rwanda (Fransolet, 1980), southwestern England (Braithwaite and Cooper, 1982), Argentina (Galliski et al., 2020), the Czech Republic (Uher et al., 1998), Brazil (da Costa et al., 2005; Karfunkel

et al., 1997), Kosovo (Bermanec et al., 1995), Kazakhstan (Ginzburg and Voroncova, 1950), and Great Britain and the USA (Drugman, 1915).

Childrenite is a hydrated iron and aluminum phosphate mineral with the ideal chemical formula  $\text{Fe}^{2+}\text{AlPO}_4(\text{OH})_2 \cdot \text{H}_2\text{O}$ , whereas eosphorite is the manganese endmember, conforming to the chemical formula  $\text{Mn}^{2+}\text{AlPO}_4(\text{OH})_2 \cdot \text{H}_2\text{O}$ . A related mineral, ernstite, contains ferric iron and  $\text{Mn}^{2+}$  and has the formula  $(\text{Mn}_{1-x}^{2+}\text{Fe}_x^{3+})\text{AlPO}_4(\text{OH})_{2-x}\text{O}_x$ , where  $0 < x < 1$  (Seeliger and Mücke, 1970). Commonly, these phosphate minerals are reported to occur together with Li minerals, such as the Li–phosphate montebbrasite ( $\text{LiAlPO}_4\text{OH}$ )

or Li-rich micas (Fransolet, 1980; Galliski et al., 2020; London and Burt, 1982; Nahodilová, 2022; Uher et al., 1998). Typically, childrenite, eosphorite, and ernstite are products of albite and K-feldspar alteration, caused by phosphorus-enriched hydrothermal solutions (Braithwaite and Cooper, 1982; Fransolet, 1980; Galliski et al., 2020; Karfunkel et al., 1997). On the other hand, the formation of ernstite at the location of its discovery near Karibib, Namibia, has been attributed to the oxidation of primary eosphorite, which itself crystallized from late-stage hydrothermal fluids in a pegmatite environment (Seeliger and Mücke, 1970). Oxidized childrenite has been reported in the literature only a few times (Fransolet, 1980; Ginzburg and Voroncova, 1950; Seeliger and Mücke, 1970; Spencer, 1952), but it is debated whether it exists in nature at all. Galliski et al. (2020) stated that the “iron-dominant equivalent of ernstite is stable in nature; this would be the first known occurrence”, with iron-dominant ernstite being considered the same phase as oxidized childrenite; the authors, however, did not present data to confirm the actual presence of  $\text{Fe}^{3+}$ . In general, eosphorite, childrenite, ernstite, and potentially  $\text{Fe}^{3+}$ -dominant childrenite (“oxychildrenite”) are difficult to distinguish based on chemical and powder X-ray data only (da Costa et al., 2005). Even when using Mössbauer spectroscopy, the distinction between these related phases may be complex due to the presence in some samples of mixtures of oxidized and non-oxidized species (da Costa et al., 2005).

Unit cell parameters and possible space groups (*Bbam* or *Bba2*) of childrenite were first reported by Barnes (1949). Giuseppetti and Tadini (1984) refined the crystal structure of childrenite in both space groups, preferring the acentric *Bba2* symmetry, owing to the ordering of H atoms. Bermanec et al. (1995), however, did not measure any piezoelectric effect, suggesting that the correct space group could be *Bbam*, although they hypothesized that the actual symmetry of childrenite is lower: either monoclinic or even triclinic. Gatta et al. (2013) refined the crystal structure of the Mn-endmember eosphorite using single-crystal neutron diffraction data. Gatta et al.’s (2013) group’s refinement was performed in the centrosymmetric space group *Cmca* instead of the acentric *C2cb* (the latter being suggested by Giuseppetti and Tadini, 1984), taking into account the transformation of the unit cell according to the matrix  $[001 | 100 | 010]$ .

In this study, we examined samples from the Homolka granite, Czech Republic, which was previously described in detail by Breiter and Scharbert (1995), Nahodilová (2022), and Uher et al. (1998). Specifically, Uher et al. (1998) reported the presence of childrenite as an accessory mineral, whereas Nahodilová (2022) provided a detailed description of mainly eosphorite, with one childrenite analysis, and several other phosphate phases. In the present study, we carried out a multi-analytical characterization of childrenite from Homolka in order to provide detailed information on its chemical composition and crystal structure, as well as the oxidation state of iron.

## 2 Geological setting

The Homolka granite forms an outcrop of 6 km<sup>2</sup> in the southern part of the Czech Republic, close to the border with Austria (Fig. 1). It is a Moldanubian (South Bohemian) granite (Breiter and Scharbert, 1995; Uher et al., 1998), intruded during the Variscan orogeny, which resulted from the collision between Gondwana and Laurasia (Kroner and Romer, 2013). While the Variscan subduction ceased at about 340 Ma, the subsequent isothermal exhumation was likely responsible for voluminous granitic magmatism and high-temperature metamorphism (Kroner and Romer, 2013). The Homolka granite has a Rb–Sr age of  $319 \pm 7$  Ma, and, on the basis of  $^{40}\text{Ar}/^{39}\text{Ar}$  data, its constituent muscovite crystals give a cooling interval between  $317 \pm 2$  and  $315 \pm 3$  Ma (Breiter and Scharbert, 1995).

Other Moldanubian granites in the southern Czech Republic have also intruded as small stocks or dikes after large volumes of two-mica granites were formed, e.g., near Nové Hradky, Sedmihoří at Domažlice, Waidhaus–Rozvadov area, Pelhřimov, and Rožmberk (Breiter and Scharbert, 1995). These Moldanubian granites are geologically the youngest granites in their respective areas, and they were intruded in a north–south orientation. They are chemically peraluminous; highly differentiated; and enriched in Li, F, P, Rb, Nb, and Sn but depleted in Fe, Mg, Ca, Sr, Ba, Zr, and rare earth elements (REEs; Breiter and Scharbert, 1995).

Major phases present in the Homolka granite are quartz, albite, K-feldspar, and Li-bearing muscovite, whereas zircon, apatite, monazite, cassiterite, and columbite occur as minor phases (Breiter and Scharbert, 1995; Uher et al., 1998). Most recently, Nahodilová (2022) provided a thorough overview of the phosphates occurring in the Homolka granite, where they make up 1 wt %–3 wt % of the whole rock; the phosphate minerals include triphylite, montebrasite, eosphorite, childrenite, vivianite, mitridatite, and a Cl- and F-bearing member of the apatite group, as well as an unidentified phase, which occurs as radial aggregates and was formed during late-stage alteration.

## 3 Materials and methods

### 3.1 Rock samples

Samples of fresh Homolka granite were collected on 11 July 2020 from two outcrops near the southern boundary of the Homolka granite body (Fig. 1). The coordinates of the two sampling sites are (1)  $49^{\circ}01.846' \text{ N}$ ,  $14^{\circ}59.323' \text{ E}$  and (2)  $49^{\circ}01.852' \text{ N}$ ,  $14^{\circ}59.391' \text{ E}$ .

### 3.2 Optical microscopy

Polished thin sections of the samples were prepared by Wagner Petrographic (Utah, USA). These thin sections were first studied by using a Leica DM4 P polarizing petrographic mi-

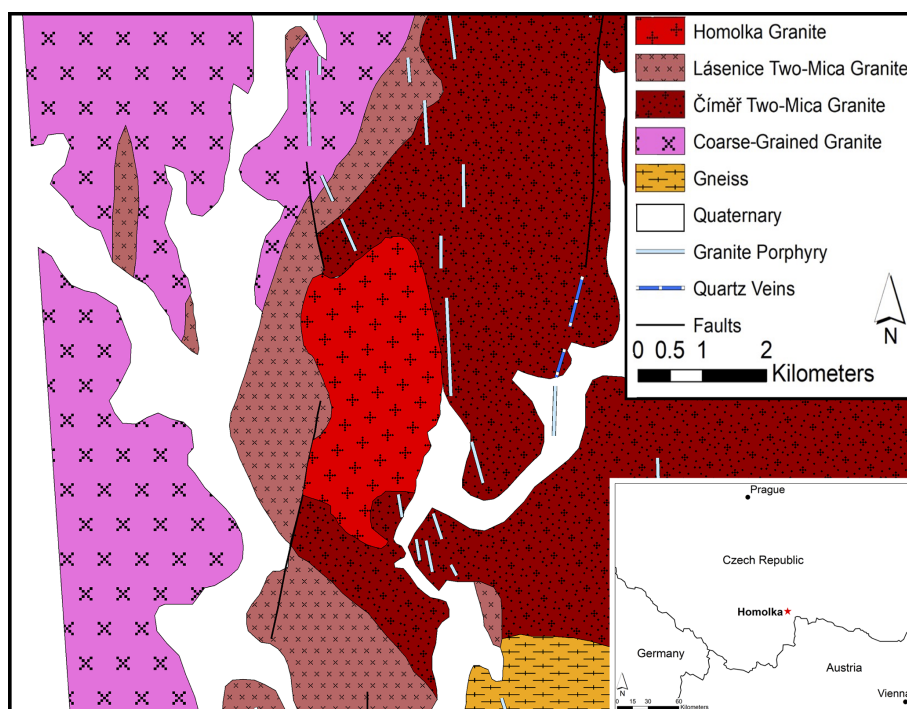


**Figure 1.** Location and geological map of the Homolka granite, adapted from Breiter and Scharbert (1995) and the 1 : 25 000 map of the Czech Geological Survey.

croscope, equipped with a digital Leica DFC550 camera to capture images using the Leica Application Suite X software (LAS X, 2020).

### 3.3 Electron microprobe analysis

The childrenite–eosphorite series minerals were analyzed by electron microprobe using a Superprobe JEOL JXA 8200, which is equipped with both energy-dispersive (EDS) and wavelength-dispersive (WDS) systems and is installed in the Eugen F. Stumpfl Laboratory at the University of Leoben, Austria. During quantitative analysis, the electron microprobe was operated in the WDS mode, with an accelerating voltage of 15 kV and a beam current of 10 nA. Counting times were 20 s on the peak and 10 s on the left and right backgrounds. All elements were analyzed using their  $K\alpha$  line, except for U, where the  $M\alpha$  line was used, and the data were processed with the ZAF (atomic number, absorption, and fluorescence) correction method. The selected standards were albite, fluorite, ilmenite, kaersutite, olivine, rhodonite, sanidine, tugtupite, uraninite, and wollastonite. The following diffracting crystals were used: TAP (thallium acid phthalate) for Na, Mg, and Al; PETJ (pentaerythritol) for K, Si, and Ca; PETH (pentaerythritol) for Cl, P, and U; LIFH (lithium fluoride) for Ti, Mn, and Fe; and LDE1 (multilayer W–Si crystal) for F. The detection limits were calculated by the Sun Solaris software, taking into account (1) average X-ray intensity of background, (2) counting time of the back-

ground signal, (3) intensity of the characteristic X-ray of the analyzed element, and (4) mass concentration in the standard sample. Detection limits are as follows (in elemental wt %): Ca (0.005); K, Mg, Mn, and Fe (0.01); Al, Si, Na, P, Cl, and Ti (0.02); F (0.05); and U (0.06). The same electron microprobe was also used to obtain backscattered electron (BSE) images, increasing the accelerating voltage to 20 kV with the same beam current of 10 nA used during electron microprobe analysis.

### 3.4 X-ray diffraction

Single-crystal X-ray diffraction (XRD) data were collected on a grain (Grain A in Fig. 2) of the childrenite series using a Bruker D8 Venture diffractometer (50 kV, 1.4 mA) equipped with an air-cooled Photon III detector and microfocus  $MoK\alpha$  radiation (Centro per l'Integrazione della Strumentazione scientifica dell'Università di Pisa, University of Pisa, Italy). The detector-to-crystal distance was set to 38 mm. Data were collected using  $\varphi$  and  $\omega$  scan modes, in  $0.5^\circ$  slices, with an exposure time of 15 s per frame. A total of 1176 frames were collected. Intensity data were integrated and corrected for Lorentz, polarization, background effects, and absorption using the software package APEX4 (Bruker, 2022). Statistical tests on  $|E|$  values ( $|E^2 - 1| = 0.908$ ) suggested the centric nature of childrenite. Crystal structure refinement was performed starting from the atomic coordinates of isotypic eosphorite (Gatta et al., 2013) using SHELXL-2018

(Sheldrick, 2015), and neutral scattering curves were taken from the *International Tables for Crystallography* (Wilson, 1992).

### 3.5 Raman spectroscopy

Micro-Raman spectra of childrenite were collected on the same grain used for single-crystal X-ray diffraction and electron microprobe analysis through a HORIBA Jobin Yvon XploRA Plus apparatus, equipped with a motorized  $x$ - $y$  stage and an Olympus BX41 microscope with a  $50\times$  objective (Dipartimento di Scienze della Terra, Università di Pisa). Raman spectra were excited using a 532 nm line of a solid-state laser, attenuated to 25 % (i.e., 6.25 mW) in order to avoid potential sample damage. The minimum lateral and depth resolutions were set to a few micrometers. The system was calibrated using the  $520.6\text{ cm}^{-1}$  Raman band of silicon before each experimental session. Spectra were collected through multiple acquisitions (three) with a single counting time of 80 s. Backscattered radiation was analyzed with a  $1200\text{ g mm}^{-1}$  grating monochromator. Experimental precision can be estimated at  $\pm 2\text{ cm}^{-1}$ .

## 4 Results and discussion

The collected rock samples are white to light gray, mostly massive, with medium-sized crystals. The Homolka granite was first studied by optical microscopy, which revealed that the rock consists primarily of quartz, muscovite, albite, and K-feldspar. During the examination of the thin sections by electron microprobe, two grains identified as childrenite were discovered. While childrenite has been reported from the Homolka granite (Nahodilová, 2022; Uher et al., 1998), it is still a rather rare mineral, and therefore, our investigation was expanded to more fully characterize this accessory phase.

The two childrenite crystals are small ( $130\times 206$  and  $170\times 220\text{ }\mu\text{m}$ , width  $\times$  length) and have a high relief compared to the surrounding feldspars and quartz (Fig. 2). The childrenite crystals also contain tiny inclusions, which are visible in both optical and BSE images (Figs. 2, 3) and probably consist of uraninite. Both crystals exhibit irregular and rounded grain boundaries and, thus, appear elliptical ( $e = (1 - b^2 \times a^{-2})^{-1} = 0.78$  and  $0.64$ , respectively, where  $b$  is the semi-minor axis and  $a$  the semi-major axis). In BSE images, the two examined crystals display patchy zoning (Fig. 3), which results largely from an uneven distribution of Fe and Mn. The brighter patches correspond to a higher Fe:Mn value compared to the darker patches. The studied grains contain on average  $21.8\pm 3.0\text{ wt \% FeO}$  (total iron) and  $8.9\pm 2.8\text{ wt \% MnO}$  (Table 1). They also host some Ca, with CaO contents varying between  $0.29\text{ wt \%}$  and  $1.62\text{ wt \%}$ , and minor amounts of Si. All major oxide concentrations are in good agreement with data from Nahodilová (2022). Including  $\text{H}_2\text{O}$  contents that correspond to the number of H

**Table 1.** Descriptive statistics of the childrenite electron microprobe analyses ( $n = 20$ ).

wt %	Average	SD	Max	Min
SiO <sub>2</sub>	0.20	0.22	0.75	< 0.04
Al <sub>2</sub> O <sub>3</sub>	21.95	0.29	22.39	21.34
FeO <sup>a</sup>	21.77	2.95	26.64	15.27
MnO <sup>b</sup>	8.92	2.77	14.57	4.06
CaO	0.79	0.36	1.62	0.29
P <sub>2</sub> O <sub>5</sub>	32.95	0.52	33.83	31.97
<hr/>				
Anhydrous total	86.57	0.73	87.89	85.41
H <sub>2</sub> O <sup>c</sup>	15.72	0.14	15.98	15.44
<hr/>				
Total	102.29	0.82	103.72	101.14
<hr/>				
Atoms per formula unit (based on three cations and seven oxygens)				
<hr/>				
Si	0.01	0.01	0.03	
Al	0.96	0.02	0.99	0.93
Fe <sup>2+</sup>	0.68	0.09	0.82	0.48
Mn <sup>2+</sup>	0.28	0.09	0.46	0.13
Ca	0.03	0.01	0.06	0.01
P	1.04	0.01	1.05	1.02
Sum	3.00			
<hr/>				
Sum (+) charges	10.09	0.03	10.15	10.03
OH <sup>c</sup>	2.09	0.03	2.15	2.03
H <sub>2</sub> O <sup>c</sup>	0.91	0.03	0.97	0.85
H <sup>c</sup>	3.91	0.03	3.97	3.85

<sup>a</sup> Total iron. <sup>b</sup> Total manganese. <sup>c</sup> Calculated to achieve electrostatic balance (based on three cations and seven oxygens per formula unit).

atoms based on three cations and seven oxygens per formula unit yields analytical totals that are greater than 100 wt % for all analyses (Table 1). These high totals suggest that childrenite experienced partial dehydration under the electron beam, consistent with the beam damage visible in the BSE images (Fig. 3). All individual electron microprobe analyses are presented in the Supplement (Table S1).

The chemical formula of childrenite from the Homolka granite, calculated on the basis of three cations per formula unit, is  $(\text{Fe}_{0.68}\text{Mn}_{0.28}\text{Ca}_{0.03})_{\Sigma 0.99}\text{Al}_{0.96}(\text{P}_{1.04}\text{Si}_{0.01})_{\Sigma 1.05}\text{O}_{4.00}(\text{OH})_{2.09}\cdot 0.91\text{H}_2\text{O}$ , with the (OH) calculated in order to achieve electrostatic balance. The  $\text{Fe}_{\text{tot}} \times (\text{Fe}_{\text{tot}} + \text{Mn})^{-1}$  values range from 0.51 to 0.86, with an arithmetic mean of 0.71 and a standard deviation of 0.09. Therefore, the grains studied here can be classified as childrenite. As shown in Fig. 4, the Mn and Fe contents determined in 20 analysis spots across the two crystals display a strong negative correlation ( $r = 0.984$ ,  $p < 0.001$ ), confirming the one-for-one substitution of  $\text{Mn}^{2+}$  for  $\text{Fe}^{2+}$  in the childrenite–eosphorite series. Nahodilová (2022), moreover, reported data that document the presence of eosphorite in the Homolka granite as well. Including the six analyses of eosphorite published

**Table 2.** Summary of crystal data and parameters describing data collection and refinement of childrenite from the Homolka granite.

Crystal data	
Crystal size (mm)	0.090 × 0.060 × 0.050
Space group	<i>Cmca</i>
<i>a</i> (Å)	6.9226(9)
<i>b</i> (Å)	10.4081(13)
<i>c</i> (Å)	13.3957(17)
<i>V</i> (Å <sup>3</sup> )	965.2(2)
<i>Z</i>	8
Data collection and refinement	
Radiation, wavelength (Å)	MoK $\alpha$ , $\lambda = 0.71073$
Temperature (K)	293(2)
$2\theta_{\max}$ (°)	56.57
Measured reflections	5682
Unique reflections	640
Reflections with $F_o > 4\sigma(F_o)$	602
$R_{\text{int}}$	0.0343
$R\sigma$	0.0208
Range of <i>h, k, l</i>	$-6 \leq h \leq 9,$ $-13 \leq k \leq 13,$ $-17 \leq l \leq 17$
$R_1 [F_o > 4\sigma(F_o)]$	0.0295
$R_1$ (all data)	0.0310
$wR_2$ (on $F_o^2$ )*	0.0717
Goof	1.174
Number of least-squares parameters	66
Maximum and minimum residual peak ( $e \text{ \AA}^{-3}$ )	+0.50 (at 0.73 Å from O1) −0.92 (at 1.16 Å from H3)

$$*w = 1/[\sigma^2(F_o^2) + (0.0277P)^2 + 5.2739P].$$

**Table 3.** Selected bond distances (in Å) and bond valence sums (in valence units, v.u.) for childrenite from the Homolka granite. Bond valence sums for the mixed Fe site were refined using the site occupancy (Fe<sub>0.68</sub>Mn<sub>0.28</sub>Ca<sub>0.03</sub>).

Fe	−O4	2.1634(19) × 2	Al	−O3	1.8497(9) × 2	P	−O2	1.529(3)
	−O2	2.2032(16) × 2		−O5	1.8927(17) × 2		−O5	1.539(2) × 2
	−O1	2.2086(16) × 2		−O4	1.9676(18) × 2		−O1	1.545(3)
	average	2.1917		average	1.9033		average	1.538
Site	O1	O2	O3	O4	O5	$\Sigma$ cations	Theor.	
Fe	2×→0.31↓×2	2×→0.31↓×2		2×→0.34		1.92	2.00	
Al			2×→0.58↓×2	2×→0.43	2×→0.52	3.06	3.00	
P	1.22	1.27			2×→1.24	4.97	5.00	
$\Sigma$ anions	1.84	1.89	1.16	0.77	1.76			
H bonds	+0.18	−	−0.18	−0.23 + 0.35 <sup>a</sup> −0.23 − 0.35 <sup>b</sup>	+0.23			
$\Sigma$ anions corr.	2.02	1.89	0.98	0.89 <sup>a</sup> 0.19 <sup>b</sup>	1.99			

<sup>a</sup> Acceptor of H bonds from O4 and donor to O5. <sup>b</sup> Donor of H bonds to O4 and O5.

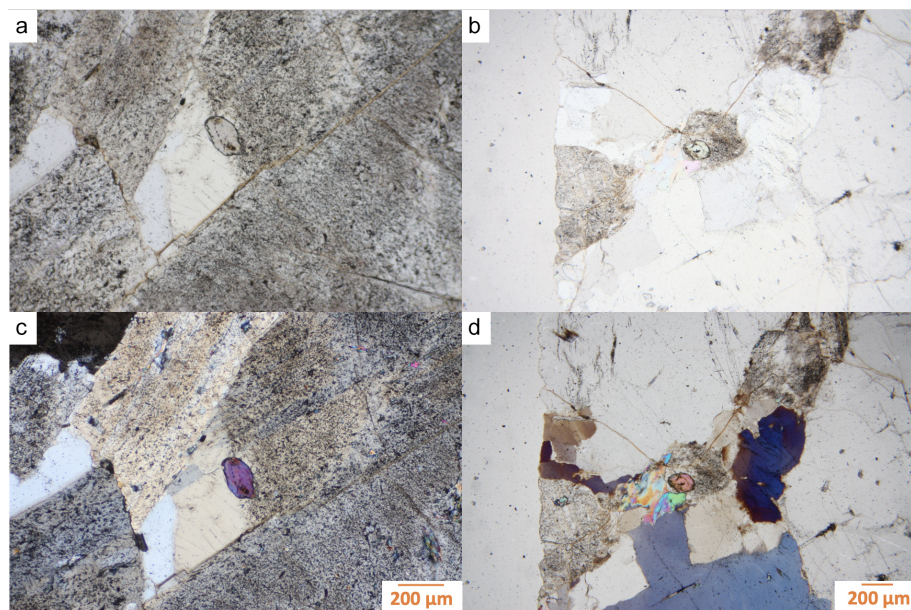


**Figure 2.** Photomicrographs of the two analyzed childrenrite crystals (in the center of the images). Panels (a) and (b) are plane-polarized light images, and panels (c) and (d) are the corresponding cross-polarized light images. Panels (a) and (c) show what we refer to as Grain A throughout the article, and panels (b) and (d) highlight Grain B.

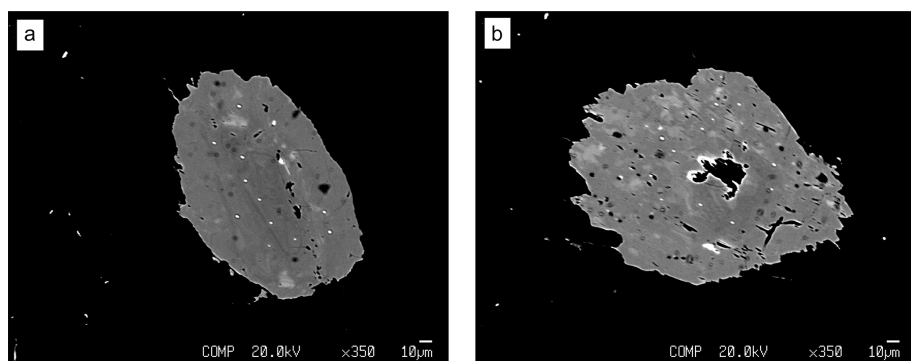


**Figure 3.** Backscattered electron images of the two childrenrite crystals, showing patchy zoning of darker and lighter material within the crystals. Panel (a) shows Grain A, and (b) shows Grain B. The darker round spots correspond to the location where the microprobe measurements were taken (beam damage).

by Nahodilová (2022) extends the Mn range to higher values (orange symbols in Fig. 4) and improves the correlation towards the theoretical 1 : 1 substitution line (slope is  $-1.05$ ,  $r = 0.99$ , intercept is  $0.995$ ,  $p < 0.001$ ). Our chemical data can stoichiometrically fit the “Fe<sup>3+</sup>-dominant ernstite” formula presented in Galliski et al. (2020; same formula as that given above); however, with only electron microprobe data, we could not constrain the valence state of Fe and had to employ single-crystal XRD and Raman spectroscopy to differentiate the two phases.

The crystal structure of childrenrite from the Homolka granite was refined according to the structural model of Gatta et al. (2013) in the *Cmca* space group. Details of data collection and structure refinements are given in Table 2.

Atomic coordinates and displacement parameters are given in the Crystallographic Information File (CIF), available in the Supplement. Selected bond distances and bond valence sums, calculated using the bond parameters of Gagné and Hawthorne (2015), are reported in Table 3. The crystal structure is formed by chains of distorted Fe-centered octahedra, connected through edge-sharing, and chains of Al-centered octahedra, both running along the **a** axis (Fig. 5). These two kinds of chains are bonded via shared corners forming {100} sheets, connected along **b** by PO<sub>4</sub> groups and H bonds, giving rise to a 3D framework.

The Fe site hosts Fe, Mn, and minor Ca. Its mean atomic number (MAN) is 25.35 electrons, compared with 25.28 electrons calculated on the basis of electron microprobe anal-

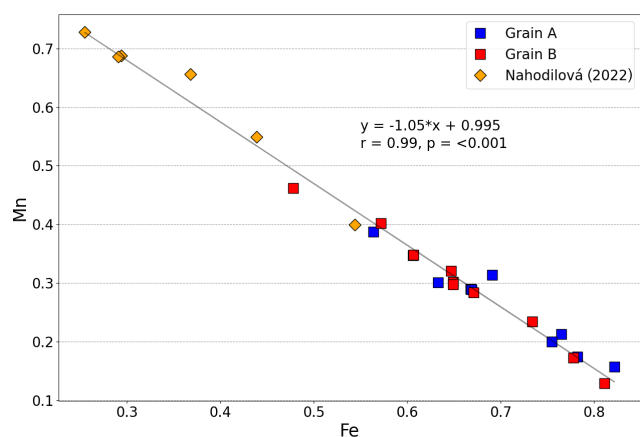


**Figure 4.** Variation in the molar Fe and Mn contents (in atoms per formula unit) in the two childrenite crystals analyzed in this study ( $n = 20$ ) as well as the six analyses reported by Nahodilová (2022, orange diamonds). The Fe value represents total iron. The displayed correlation line and its equation were calculated by including all 20 data points from the two crystals analyzed here and the 6 analyses published by Nahodilová (2022).

ysis. The average bond distance of 2.192 Å at the Fe site is slightly larger than that observed by Giuseppetti and Tadini (1984), i.e., 2.187 Å, and smaller than the value observed by Gatta et al. (2013) in eosphorite, i.e., 2.219 Å. These differences are related to the  $\text{Fe}_{\text{tot}} \times (\text{Fe}_{\text{tot}} + \text{Mn})^{-1}$  ratio of the studied samples, i.e., 0.71, 0.89, and 0.06 for the specimens from the Homolka granite (this study), Tavistock (Giuseppetti and Tadini, 1984), and Chamachu (Gatta et al., 2013), respectively. As the ionic radius of  $^{\text{VI}}\text{Mn}^{2+}$  is larger than that of  $^{\text{VI}}\text{Fe}^{2+}$  (0.83 vs. 0.78 Å, respectively; Shannon, 1976), the occurrence of more Mn is related to larger average distances at the Fe-centered site. The bond valence sum at the Fe site, 1.92 valence units (v.u.; Table 2), agrees with the occupancy of this site by divalent cations. The Al site is a pure Al site, in agreement with chemical data (Table 1). Its average bond distance is 1.903 Å, consistent with data given by Giuseppetti and Tadini (1984) and Gatta et al. (2013) for childrenite and eosphorite, respectively. The bond valence sum at the Al site is 3.06 v.u., in accordance with the occurrence of  $\text{Al}^{3+}$ . Finally, the P tetrahedral site was refined as a pure P position. The average bond distance of 1.538 Å agrees with the grand value given by Huminicki and Hawthorne (2002) for  $\langle \text{P}-\text{O} \rangle$  distance, i.e., 1.537 Å. The bond valence sum is 4.97 v.u., consistent with the presence of  $\text{P}^{5+}$  at this site. Two out of the five independent O sites are underbonded, i.e., O3 and O4. The location of the H atoms confirms the previous H-bonding scheme described by Gatta et al. (2013). In Table 3, the bond valence sums of the O site are corrected by calculating the bond strength of the H bonds according to the relations of Ferraris and Ivaldi (1988). The O4 site statistically hosts  $\text{H}_2\text{O}$  and OH groups, whereas O3 is a site with

OH groups only; O1, O2, and O5 are represented by  $\text{O}^{2-}$  anions.

Crystal structure data can be useful for the interpretation of the micro-Raman spectrum of childrenite. In Fig. 6, the spectrum of childrenite from the Homolka granite is compared with those reported in the RRUFF database for a sample from the George and Charlotte Mine (Tavistock, Devon, England), previously characterized using single-crystal XRD and chemical analyses (Lafuente et al., 2016). The two Raman spectra, in the range between 200 and 1300  $\text{cm}^{-1}$ , are in good agreement (Fig. 6a). In accordance with Frezzotti et al. (2012) and Litasov and Podgornykh (2017), the strong Raman band centered at 966  $\text{cm}^{-1}$  and the bands at 1011 and 1045  $\text{cm}^{-1}$  are due to the symmetric ( $\nu_1$ ) and antisymmetric ( $\nu_3$ ) stretching modes of the  $\text{PO}_4$  group, respectively. The bending modes ( $\nu_2$  and  $\nu_4$ ) of the  $\text{PO}_4$  group occur in the range between 300 and 650  $\text{cm}^{-1}$ . The weak bands below 300  $\text{cm}^{-1}$  may be attributed to lattice modes and/or to the Fe, Ca, and Al–O vibration modes. The O–H stretching region, between 2000 and 4000  $\text{cm}^{-1}$ , is characterized by several broad and intense bands, according to the key role played by H bonds in the childrenite crystal structure. In this spectral region (Fig. 6b), the strong Raman band is centered at 3435  $\text{cm}^{-1}$ . We would like to stress that the difference observed in the O–H stretching region between the Homolka and the RRUFF data is due to the glue used for the preparation of the thin section of the studied samples (Fig. 6b). No bending mode due to the occurrence of  $\text{H}_2\text{O}$  groups was observed in the region between 1400 and 1700  $\text{cm}^{-1}$ .

The structural and spectroscopic data do not agree with those reported by Frost et al. (2013), who suggested the occurrence of  $\text{PO}_4$ ,  $\text{PO}_3(\text{OH})$ , and  $\text{PO}_2(\text{OH})_2$  groups in the Mn-isotope eosphorite, probably related to the cation vacancies at the (Fe/Mn)-bearing site; on the basis of their spectroscopic and chemical data, they proposed a revision of the chemical formula of the series childrenite–eosphorite to  $(\text{Mn},\text{Fe})\text{Al}(\text{PO}_4,\text{OHPO}_3)(\text{OH})_2 \cdot (\text{H}_2\text{O})$ . However, their interpretation was not supported by single-crystal data of eosphorite (see Gatta et al., 2013) or by the current study on childrenite.

## 5 Conclusions

Childrenite is a relatively rare phosphate mineral, which typically forms during alteration of highly evolved granites and pegmatites. It was identified in the highly evolved and altered Homolka granite in the Czech Republic. The electron microprobe data for the two studied crystals highlight the observed patchy zoning and provide good statistical data for the Fe-for-Mn substitution. All our analyses show  $\text{Fe} > \text{Mn}$ , therefore belonging strictly to childrenite composition and extending the solid solution from this locality reported by Nahodilová (2022). We also refined the crystal structure of childrenite using single-crystal XRD data, agreeing with the

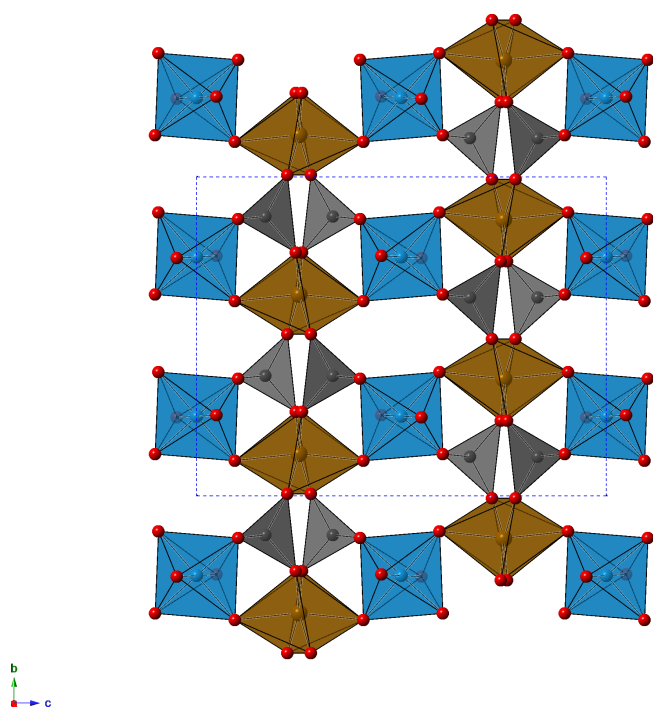


**Figure 5.** Crystal structure of childrenite as seen down **a**. Brown, light blue, and gray polyhedra represent Fe, Al, and P sites, respectively. Red circles represent O atoms. For the sake of clarity, H atoms are not shown.

Gatta et al. (2013) structural model. Our analysis confirms the presence of  $\text{Fe}^{2+}$  only at the Fe site, as the bond valence sum at that site is 1.92 valence units. The combination of electron probe microanalysis and XRD techniques was paramount to achieve proper identification since the chemical composition of childrenite without differentiation of the Fe valence state is quite similar to that of “oxychildrenite”/ $\text{Fe}^{3+}$ -dominant ernstite. Using the single-crystal XRD data allowed us to discriminate the presence of  $\text{Fe}^{2+}$  from  $\text{Fe}^{3+}$  and, as a consequence, to avoid an erroneous classification of the studied crystals, based only on electron microprobe data. The Raman spectra fit well with the RRUFF database of childrenite.

**Data availability.** All data attached to the article are presented either in the supplementary table or in the tables within the text. The data referenced can be accessed directly from the tables within the text of Nahodilová (2022; <https://doi.org/10.3140/zpravy.geol.2022.06>).

**Supplement.** The supplement related to this article is available online at: <https://doi.org/10.5194/ejm-36-1-2024-supplement>.

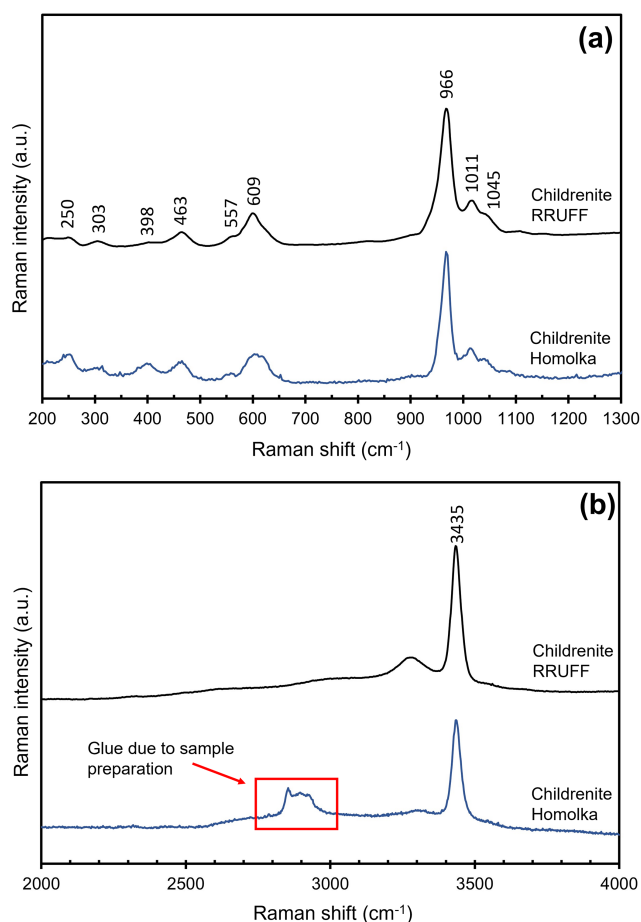


**Figure 6.** Raman spectrum of childrenite from the Homolka granite compared with data given in the RRUFF project (Lafuente et al., 2015) in the regions between 200 and  $1300\text{ cm}^{-1}$  (a) and  $2000\text{--}4000\text{ cm}^{-1}$  (b).

**Author contributions.** JT collected the samples, lead initial investigations of the samples, and wrote the manuscript with contributions from all authors. CB collected the single-crystal XRD data, DM the Raman spectra, and FZ the electron microprobe data. RG conceptualized, guided, and supervised the study and provided feedback during the data collection and writing stages.

**Competing interests.** At least one of the (co-)authors is a member of the editorial board of *European Journal of Mineralogy*. The peer-review process was guided by an independent editor, and the authors also have no other competing interests to declare.

**Disclaimer.** Publisher’s note: Copernicus Publications remains neutral with regard to jurisdictional claims made in the text, published maps, institutional affiliations, or any other geographical representation in this paper. While Copernicus Publications makes every effort to include appropriate place names, the final responsibility lies with the authors.

*Acknowledgements.* We thank Karel Breiter for suggesting interesting sites to visit and sample early in the conceptualization of our study. The Centro per l'Integrazione della Strumentazione scientifica dell'Università di Pisa (C.I.S.U.P.) is thanked for the access to the single-crystal X-ray diffraction laboratory.

*Financial support.* This study was partially supported by grant P30-ES013508 awarded by the National Institute of Environmental Health Sciences (NIEHS). The findings are not the official opinions of NIEHS or NIH. This work was also supported by the University of Pennsylvania (Benjamin Franklin Fellowship).

*Review statement.* This paper was edited by Rossella Arletti and reviewed by two anonymous referees.

## References

- Barnes, W. H.: The Unit Cell and Space Group of Childrenite, *Am. Mineral.*, 34, 12–18, 1949.
- Bermanec, V., Šćavničar, S., and Zebec, V.: Childrenite and crandalite from the Stari Trg mine (Trepfia), Kosovo: new data, *Miner. Petrol.*, 52, 197–208, 1995.
- Braithwaite, R. S. W. and Cooper, B. V.: Childrenite in South-West England, *Mineral. Mag.*, 46, 119–126, 1982.
- Breiter, K. and Scharbert, S.: The Homolka magmatic centre – an Example of Late Variscan ore bearing magmatism in the Southbohemian Batholith (Southern Bohemia, Northern Austria), *Jahrbuch der Geologischen Bundesanstalt*, 138, 9–25, 1995.
- Brooke, H. J. A.: *Quarterly Journal of Science, Literature and the Arts*, Royal Institute of Great Britain, 16, 274–275, 1823.
- Bruker, S.: Bruker AXS Inc, <https://www.bruker.com/ProductDetail/9269> (last access: 20 December 2023), 2022.
- Bush, G. J. and Dana, E. S.: On a new and remarkable mineral locality in Fairfield County, Connecticut, with a description of several new mineral species occurring there, *Am. J. Sci.*, 16, 114–123, 1878.
- da Costa, G. M., Scholz, R., Karfunkel, J., Bermanec, V., and de Sá Carneiro Chaves, M. L.:  $^{57}\text{Fe}$ -Mössbauer spectroscopy on natural eosphorite-childrenite-ernstite samples, *Phys. Chem. Miner.*, 31, 714–720, 2005.
- Drugman, J.: On Childrenite from Crinnis mine, Cornwall, and Eosphorite from Poland, Maine, *Mineral. Mag. J. M. Soc.*, 17, 193–201, 1915.
- Ferraris, G. and Ivaldi, G.: Bond valence vs bond length in  $\text{O}\cdots\text{O}$  hydrogen bonds, *Acta Crystallogr.*, 44, 341–344, 1988.
- Fransolet, A. M.: The eosphorite-childrenite series associated with the Li-Mn-Fe phosphate minerals from the Buranga pegmatite, Rwanda, *Mineral. Mag.*, 43, 1015–1023, 1980.
- Frezzotti, M., Tecce, F., and Casagli, A.: Raman spectroscopy for fluid inclusion analysis, *J. Geochem. Explor.*, 112, 1–20, 2012.
- Frost, R. L., Xi, Y., Scholz, R., López, A., Lima, R. M. F., and Ferreira, C. M.: Vibrational spectroscopic characterization of the phosphate mineral series eosphorite-childrenite- $(\text{Mn,Fe})\text{Al}(\text{PO}_4)(\text{OH})_2\cdot(\text{H}_2\text{O})$ , *Vib. Spectrosc.*, 67, 14–21, <https://doi.org/10.1016/j.vibspec.2013.03.005>, 2013.
- Gagné, O. C. and Hawthorne, F. C.: Comprehensive derivation of bond-valence parameters for ion pairs involving oxygen, *Acta Crystallogr. B*, 71, 562–578, <https://doi.org/10.1107/S2052520615016297>, 2015.
- Galliski, M. A., Roda-Robles, E., Hatert, F., Márquez-Zavallá, M. F., and Martínez, V. A.: The phosphate mineral assemblages from La Viquita Pegmatite, San Luis, Argentina, *Can. Mineral.*, 58, 733–746, 2020.
- Gatta, G. D., Nenert, G., and Vignola, P.: Coexisting hydroxyl groups and  $\text{H}_2\text{O}$  molecules in minerals: A single-crystal neutron diffraction study of eosphorite,  $\text{MnAlPO}_4(\text{OH})_2\cdot\text{H}_2\text{O}$ , *Am. Miner.*, 98, 1297–1301, <https://doi.org/10.2138/am.2013.4438>, 2013.
- Ginzburg, A. and Voroncova, N. V.: Oxychildrenite a new mineral of the iron-manganese-aluminium phosphate group, *Dokladi Akademii Nauk SSSR*, 72, 145–148, 1950.
- Giuseppetti, G. and Tadini, C.: The crystal structure of childrenite from Tavistock (SW England), Ch89Eo11 term of childrenite-eosphorite series, *Neues Jahrbuch für Mineralogie, Monatshefte*, 263–271, 1984.
- Humnicki, D. M. C. and Hawthorne, F. C.: The crystal chemistry of phosphate minerals, *Rev. Miner. Geochem.*, 48, 123–253, 2002.
- Hurlbut Jr., C. S.: Childrenite-eosphorite series, *Am. Miner.*, 10, 793–805, 1950.
- Karfunkel, J., Chaves, M. L. S. C., Banko, A., and Irran, E.: Ernstite and eosphorite from Minas Gerais, Brazil, *Mineral. Rec.*, 28, 489–493, 1997.
- Kroner, U. and Romer, R. L.: Two plates – Many subduction zones: The Variscan orogeny reconsidered, *Gondwana Res.*, 24, 298–329, 2013.
- Lafuente, B., Downs, R. T., Yang, H., and Stone, N.: The power of databases: the RRUFF project, in: *Highlights in Mineralogical Crystallography*, Berlin, 1–30, <https://doi.org/10.1515/9783110417104-003>, 2016.
- LAS X: Leica Application Suite X, <https://www.leica-microsystems.com/products/microscope-software/p/leica-las-x-ls/> (last access: 20 December 2023), 2020.
- Litasov, K. D. and Podgornykh, N. M.: Raman spectroscopy of various phosphate minerals and occurrence of tuite in the Elga IIE iron meteorite, *J. Raman Spec.*, 48, 1518–1527, 2017.
- London, D. and Burt, D. M.: Alteration of spodumene, montebrazite and lithiophilite in pegmatites of the White Picacho District, Arizona, *Am. Miner.*, 67, 97–113, 1982.
- Nahodilová, R.: Lithium-bearing phosphates and micas in Homolka leucogranite [data set], *Geosci. Res. Rep.*, 55, 41–50, <https://doi.org/10.3140/zpravy.geol.2022.06>, 2022.
- Seeliger, E. and Mücke, A.: Ernstit, ein neues  $\text{Mn}^{2+}$ - $\text{Fe}^{3+}$ -Al-phosphat und seine beziehungen zum eosphorit, *Neues Jahrbuch für Mineralogie, Monatshefte*, 289–298, 1970.
- Shannon, R. D.: Revised effective ionic radii and systematic studies of interatomic distances in halides and chalcogenides, *Acta Crystallogr.*, 32, 751–767, 1976.
- Sheldrick, G. M.: Crystal Structure Refinement with SHELXL, *Acta Crystallogr.*, 71, 3–8, 2015.
- Spencer, L. J.: Nineteenth list of new mineral names, *Mineral. Mag. J. M. Soc.*, 29, 974–998, 1952.
- Uher, P., Breiter, K., Klečka, M., and Pivec, E.: Zircon in highly evolved Hercynian Homolka granite, Moldanubian zone, Czech

Republic: Indicator of magma source and petrogenesis, *Geol. Carpath.*, 49, 151–160, 1998.

Wilson, A. J. C.: *International Tables for Crystallography*, Kluwer, Dordrecht, The Netherlands, ISBN 978-0-470-71029-6, 1992.